A finite element approach to the simulation of hydraulic fractures with lag

Michael J. Hunsweck[1], Yongxing Shen[2] and Adrian J. Lew[1,*,†]

[1]*Department of Mechanical Engineering, Stanford University, Stanford, CA, USA*
[2]*Laboratori de Càlcul Numèric, Universitat Politècnica de Catalunya (UPC BarcelonaTech), Barcelona, Spain*

SUMMARY

We presented a finite-element-based algorithm to simulate plane-strain, straight hydraulic fractures in an impermeable elastic medium. The algorithm accounts for the nonlinear coupling between the fluid pressure and the crack opening and separately tracks the evolution of the crack tip and the fluid front. It therefore allows the existence of a fluid lag. The fluid front is advanced explicitly in time, but an implicit strategy is needed for the crack tip to guarantee the satisfaction of Griffith's criterion at each time step. We enforced the coupling between the fluid and the rock by simultaneously solving for the pressure field in the fluid and the crack opening at each time step. We provided verification of our algorithm by performing sample simulations and comparing them with two known similarity solutions. Copyright © 2012 John Wiley & Sons, Ltd.

KEY WORDS: finite element; hydraulic fracture; fluid lag

1. INTRODUCTION

Hydraulic fracturing is involved in very diverse applications, ranging from the flow of magma through the earth's crust to the failure of dams due to underwater cracks [1, 2]. However, perhaps the most relevant and most investigated use of hydraulic fracturing today is in its application to the extraction of natural gas from shale [3]. In this case, water at high pressure is pumped several miles through the earth's crust through a predrilled borehole. When the water reaches the pay-zone layer where the natural gas is trapped, cracks are formed in the rock. Then, before the applied pressure is completely released, a treatment of proppant (sand slurry, etc.) is inserted into the newly formed cracks to prevent them from completely closing. Afterwards, the freed natural gas can flow back up the borehole for collection.

Numerically solving the equations that model the hydraulic fracturing process can be difficult. It is known that when the toughness of the rock is large, the fluid travels very close behind the crack tip, and it can be assumed that the crack tip and the fluid front propagate together [4–6]. However, for small toughness, the fluid lag (i.e. the gap between the fluid front and the crack tip) can be significant, so the fluid occupies only part of the crack length [5, 6]. Because both the boundary of the solid and the domain of the fluid are evolving in time, it is necessary to use a different spatial discretization for each time step in the simulation. This can be particularly challenging in the general case where the crack path is not known *a priori* because it would be necessary to ensure a suitable mesh on the evolving crack surface to solve the lubrication equations that describe the fluid in its interior.

The two-dimensional plane-strain Khristinaovic–Geertsma–de Klerk (KGD) model is widely used for the geometry of hydraulic fracture problems, where the borehole is treated as a line source in the

*Correspondence to: Adrian J. Lew, Department of Mechanical Engineering, Durand 207, 496 Lomita Mall, Stanford, CA 94305-4040, USA.
†E-mail: lewa@stanford.edu

direction out of the plane [7, 8]. For this geometry, the nature of the hydraulic fracture problem in the region of the crack tip has been analyzed by considering a crack propagating at a constant velocity in a semi-infinite medium [9–11]. For a crack of finite size with constant inlet flow rate, asymptotic solutions have been obtained in the limit of large viscosity [12, 13] and large toughness [14]. In addition, two similarity solutions have been obtained by numerically solving the governing equations. The first was obtained by Spence and Sharp [4], who derived a similarity solution by neglecting the fluid lag, which is an appropriate assumption in the asymptotic limit of late time. The second was obtained by Garagash [5], whose similarity solution is applicable for the case of zero far-field stress, which can also be interpreted as an early-time solution.

An overview of the methods used to simulate hydraulic fracturing has been given by Adachi *et al.* [3], and we will summarize some of that discussion here. Many of the first hydraulic fracture simulations were carried out based on the Perkins–Kern–Nordgren geometry, which assumes a limited crack height in the vertical direction and that the vertical cross section is elliptical [15, 16]. Clifton *et al.* [17–19] pioneered these types of planar three-dimensional simulations. Since then, several other simulations of this type have been carried out, especially in the investigation of the effects of layered media [20–22]. The prevailing method used in simulating hydraulic fractures has been the displacement discontinuity method, which is a type of boundary element method [23]. For the KGD geometry, Lecampion and Detournay [6] have devised an algorithm using the displacement discontinuity method that simulates hydraulic fracturing between the known similarity regimes at early and late time.

Although the boundary element method is widely used to investigate the hydraulic fracture problem, there are many types of hydraulic fracture problems where using finite-element-based algorithms could be especially attractive. An example of this would be when strong plastic deformation is present, or when the rock exhibits a high degree of poroelastic behavior [24–26]. In those cases, boundary element methods are not so attractive because of the transient and inhomogeneous nature of the problem. Along this line, Lecampion [27] recently investigated how to use the extended finite element method to accurately approximate the hydraulic fracture solution in the region of the crack tip at a given instant in time. In that article, it was assumed that either the crack opening or the fluid pressure was given, so that the nonlinear coupling between them was not considered. In addition, Dahi-Taleghani [28] formulated an extended-finite-element-based method to investigate intersecting fractures. In that work, it was assumed that the fluid lag was negligible.

In this article, we create a finite-element-based algorithm that evolves both the fluid front and the crack tip in time. We model the rock as an impermeable homogeneous finite linear elastic block. The two-dimensional plane-strain KGD model is adopted for the geometry. The fluid is assumed to be incompressible, laminar, and Newtonian. We also assume that lubrication theory is valid because of the smallness of the crack opening relative to the crack length, so the governing equations for the fluid are stated in a one-dimensional domain. No leak-off term is considered. The crack is assumed to propagate in a way that satisfies Griffith's criterion at all times. Under this model, it is assumed that when the fracture propagates, it does so quasi-statically such that the stress intensity factor (SIF) equals the fracture toughness.

A crucial assumption we made herein is that the fracture propagates along a predefined straight line. As mentioned, cracks propagating in arbitrary directions need a strategy to approximate the solution to the lubrication equations on the crack surface as the crack evolves. For straight cracks, this problem is noticeably simpler, although some important aspects remain. A key one is that it is necessary to iterate over the crack tip position to satisfy Griffith's criterion. In other words, it is necessary to iterate over the geometry, and hence the mesh, of the problem. In contrast, the fluid front can (generally) be advanced explicitly. A second important aspect is that fine enough meshes near the crack tip are needed when it is close to the fluid front, to resolve the steep pressure gradients induced by the small crack opening near the tip. For simplicity, we also assumed that the fluid front never reaches the crack tip because some additional care is needed to deal with the contact conditions in such situations. Of course, it could be argued that all these simplifying assumptions severely restrict the applicability of the algorithm. However, we regard the contributions herein as necessary steps toward constructing a thorough finite-element-based hydraulic fracturing strategy.

This article is organized as follows. In Section 2, we outline the problem statement and introduce the governing equations. In Section 3, we construct the algorithm by first discretizing the problem in time

and then in space. This involves introducing approximations for the time derivatives of the crack opening and the fluid front location. The resulting semidiscrete problem is independent of the spatial approximation adopted. This is a convenient feature because the finite element spaces generally change at each time step, as the geometry of the problem evolves. In Section 4, we make a specific choice for the finite element space at each time step, and we also clearly outline the specific approximations and methods used to implement the algorithm. In Section 5, we verify the proposed method by comparing the simulations it generates to two known similarity solutions [4, 5].

2. PROBLEM STATEMENT

In this article, we adopt the following model problem to construct and test a numerical method for hydraulic fractures. We restrict our attention to two-dimensional plane-strain problems in which the crack geometry is that of the KGD model [7, 8]. This consists of a single vertical planar crack, represented as a segment in the horizontal plane shown in Figure 1. A fluid is injected at a constant flow rate Q_0 through a vertical borehole located at the midpoint of the segment in Figure 1. We assume the radius of the borehole is much smaller than the crack length so that the injected fluid can be modeled as a point source. The crack then is restricted to grow symmetrically with respect to the borehole while remaining planar at all times. The crack opening is assumed to be perpendicular to the minimum far-field confining stress. To a first approximation, the minimum far-field stress is of the same order of magnitude as the maximum far-field stress, so it is standard to assume that the entire far-field stress is that of a uniform compressive far-field stress σ_0. In addition, at this stage, we assume that the fluid front never reaches the crack tip.

We introduce a Cartesian coordinate system (x_1, x_2) and define the straight crack as $(-a, a) \times \{0\}$. The fluid partially fills the crack and exists in the domain $(-L, L) \times \{0\}$ where $L < a$. We approximate the infinite medium as a finite square block of size $2s$ with $s \gg a$. Then, by taking advantage of the symmetries of the problem, only the top-right quarter of the block is considered. The computational domain is therefore $\mathcal{B} \equiv (0, s) \times (0, s)$, as shown in Figure 2, with the crack residing partway along the bottom edge. We provide computational evidence of the validity of approximating the infinite medium with a finite block in Appendix A.

The rock is characterized by its Young's modulus E, Poisson's ratio ν, and Mode I fracture toughness K_{Ic}. The fluid is characterized by its dynamic viscosity μ. We introduce the following reduced parameters:

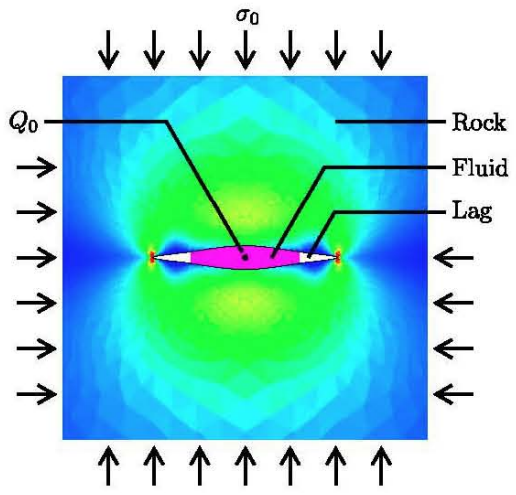

Figure 1. Basic geometry of the problem. A fluid is injected into the rock at a constant flow rate Q_0. The crack opens perpendicular to the minimum far-field stress σ_0. There is a lag region between the fluid front and the crack tip.

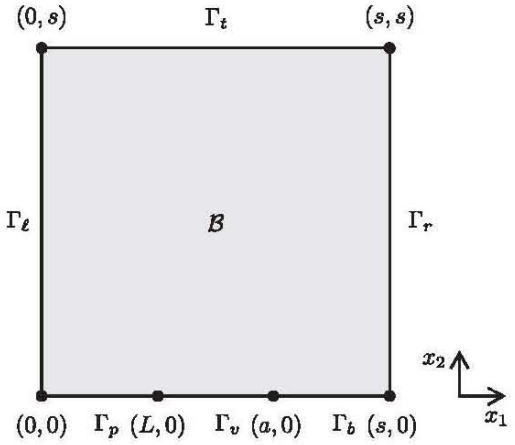

Figure 2. The top-right quarter block, which defines the computational domain $\mathcal{B}$. The crack lies along $\Gamma_p \cup \Gamma_v$, and the fluid lies in Γ_p.

$$E' = \frac{E}{1-\nu^2}, \quad K_c' = \frac{8}{\sqrt{2\pi}} K_{Ic}, \quad \mu' = 12\mu \tag{1}$$

The parameter E' is the plane-strain modulus, and the other parameters are introduced to reduce numerical clutter as well as to be consistent with a large number of articles already in the literature [10, 5, 6, 29, 27]. Note that for an infinite elastic medium, the elastic response of the solid depends on E and ν only through the combination E'. We will choose a value of $\nu = 0.3$ throughout this analysis.

The solution of the hydraulic fracture problem consists of finding the crack length $a(t)$, the fluid front $L(t)$, the rock displacement field $u(\mathcal{B}, t)$, and the fluid pressure $p(\Gamma_p, t)$, for a given set of material parameters Q_0, σ_0, E', K_c', and μ'. Here we let u_i denote the component of the displacement vector u in the Cartesian coordinate direction x_i. We should emphasize that the boundaries Γ_p, Γ_v, and Γ_b as defined in Figure 2 are functions of time because they are dependent on the two fronts, $L(t)$ and $a(t)$. In particular, this means that the domain of the fluid $\Gamma_p \equiv (0, L(t)) \times \{0\}$ also depends on time. The governing equations, at each instant in time, consist of elastostatics for the rock, and lubrication theory for the fluid, along with a set of boundary conditions for each of them. We note that the equations for the rock and the fluid are coupled because the elastic response depends on the fluid pressure, and the fluid pressure depends on the crack opening. The system evolves forward in time through the propagation of the fluid front and the crack tip, starting from a given initial condition. We detail the governing equations next.

2.1. *The rock*

We model the rock as an isotropic linear elastic material undergoing small deformations. We do not consider the effect of gravity because it is assumed to act in the direction orthogonal to the plane, and hence it is orthogonal to the motion of the fluid. We assume that, at each instant in time, the deformation is quasi-static. Consequently, the following governing equations should be satisfied at each instant in time. The equilibrium and constitutive equations are given by

$$\left.\begin{aligned} \sigma_{ij,j} &= 0 \\ \sigma_{ij} &= \mathbb{C}_{ijkl} u_{k,l} \end{aligned}\right\} \text{in } \mathcal{B} \tag{2}$$

The primary unknown of the rock is the displacement vector u, whereas the stress tensor σ can be eliminated as an unknown by combining the previous equations. We use repeated indices to imply

summation from 1 to 2, and the comma denotes partial differentiation with respect to the corresponding spatial coordinate. The fourth-order elasticity tensor $\mathbb{C}$ is known and is expressed as

$$\mathbb{C}_{ijkl} = \frac{\nu E}{(1+\nu)(1-2\nu)}\delta_{ij}\delta_{kl} + \frac{E}{2(1+\nu)}\left(\delta_{ik}\delta_{jl} + \delta_{il}\delta_{jk}\right) \tag{3}$$

where δ_{ij} is the Kronecker delta. The boundary conditions can be prescribed by specifying either the displacement u or the traction $t_i \equiv \sigma_{ij}n_j$, where n is the outer normal to $\partial\mathcal{B}$. The symmetric treatment along the bottom and left sides implies

$$\left.\begin{aligned} u_2 &= 0 \\ t_1 &= 0 \end{aligned}\right\} \text{on } \Gamma_b \equiv (a, s) \times \{0\} \tag{4}$$

$$\left.\begin{aligned} u_1 &= 0 \\ t_2 &= 0 \end{aligned}\right\} \text{on } \Gamma_\ell \equiv \{0\} \times (0, s) \tag{5}$$

and we impose the far-field stress along the top and right sides, so that

$$\left.\begin{aligned} t_1 &= 0 \\ t_2 &= -\sigma_0 \end{aligned}\right\} \text{on } \Gamma_t \equiv (0, s) \times \{s\} \tag{6}$$

$$\left.\begin{aligned} t_1 &= -\sigma_0 \\ t_2 &= 0 \end{aligned}\right\} \text{on } \Gamma_r \equiv \{s\} \times (0, s) \tag{7}$$

On the crack face, the normal traction is equal to the fluid pressure p, which is an unknown. The traction from the fluid shear stress is assumed to be negligible because, under the lubrication assumption, it is generally much smaller than the pressure. In addition, there is no traction in the lag region. These conditions imply

$$\left.\begin{aligned} t_1 &= 0 \\ t_2 &= p \end{aligned}\right\} \text{on } \Gamma_p \equiv (0, L) \times \{0\} \tag{8}$$

$$\left.\begin{aligned} t_1 &= 0 \\ t_2 &= 0 \end{aligned}\right\} \text{on } \Gamma_v \equiv (L, a) \times \{0\} \tag{9}$$

2.2. *The fluid*

Under lubrication theory, the velocity profile of the fluid at each point in the crack is that of a planar Poiseuille flow between two parallel plates, in such a way that the continuity equation is satisfied at each instant in time (see, e.g. [30]):

$$\left.\begin{aligned} 0 &= 2\dot{u}_2 + q_{,1} \\ q &= -\frac{1}{\mu'}(2u_2)^3 p_{,1} \end{aligned}\right\} \text{on } \Gamma_p \tag{10}$$

Here, q denotes the flow rate and a dot $(\cdot)$ over a quantity means the partial derivative with respect to time t at fixed spatial locations. Because of the symmetries of the problem, the crack opening $2u_2$ is equal to twice the displacement in the vertical direction u_2. The flow rate q can be eliminated by combining the previous equations. The boundary conditions consist of a constant flow rate Q_0 at the

inlet, half of which travels into the right wing of the crack,

$$q(0) = \frac{1}{2} Q_0 \tag{11}$$

At the fluid front L, the pressure must balance the vapor pressure in the fluid lag, which is assumed to be negligible, thus yielding a zero-pressure condition there, namely,

$$p(L) = 0 \tag{12}$$

2.3. *Fluid front propagation*

The time evolution of L is obtained by computing its time derivative $\dot{L}$, which is given by the mean velocity of the fluid at L:

$$\dot{L} = \left. \frac{q}{2u_2} \right|_{x_1 - L} \tag{13}$$

This is equivalent to computing the fluid front evolution from mass conservation.

2.4. *Crack tip propagation*

We used Griffith's criterion to model crack propagation. Under this model, the (reduced) SIF K' is the sole parameter governing fracture.[‡] When K' is less than the fracture toughness K_c', then the crack does not propagate. However, when the crack does propagate, it does so in a manner such that K' equals the fracture toughness K_c'. This can be summarized as follows:

$$\begin{cases} \dot{a} = 0, K' < K_c' \\ \dot{a} > 0, K' = K_c' \end{cases} \tag{14}$$

There are many different methods for computing the SIF K', which is a function of the displacement u and the pressure p. We will use a method based on computing an interaction integral [31–33]. When computing K', we must also account for the nonzero traction arising from the pressure on the crack faces. In this method, the approximation for K' is

$$K' = \frac{4}{\pi(1-\nu)} \left(I_u + I_p \right) \tag{15}$$

where I_u and I_p are given by

$$I_u = \int_{\mathcal{B}} \left[\left(\sigma_{im}^{\psi} u_{i,j} + \sigma_{im} \psi_{i,j} \right) e_j - \sigma_{ij} \psi_{i,j} e_m \right] \chi_{,m} \, d\mathcal{B}, \tag{16}$$

$$I_p = \int_{\Gamma_p} (p\chi)_{,1} \psi_2 \, d\Gamma \tag{17}$$

Here e is the unit vector tangential to the crack face at the crack tip and pointing toward the uncracked material. For our problem, we therefore have $e_i = \delta_{i1}$.

[‡]As with K_{Ic}, $K' = 8K_I/\sqrt{2\pi}$ is the reduced SIF.

The quantities ψ_1 and ψ_2 are the Cartesian components of an auxiliary displacement field ψ undergoing purely mode I fracture:

$$\psi_1 = r^{1/2}\cos\left(\frac{\theta}{2}\right)(\kappa - \cos\theta), \quad \psi_2 = r^{1/2}\sin\left(\frac{\theta}{2}\right)(\kappa - \cos\theta) \tag{18}$$

where $\kappa = 3 - 4\nu$ for plane-strain problems. The corresponding auxiliary stress field is given by $\sigma_{ij}^{\psi} \equiv \mathbb{C}_{ijkl}\psi_{k,l}$.

Finally, χ is a scalar field defined over the domain $\mathcal{B}$ such that χ satisfies some minimal smoothness assumptions and $\chi = 0$ on the boundary $\Gamma_\ell \cup \Gamma_t \cup \Gamma_r$ and also $\chi = 1$ at the crack tip $(a, 0)$. We are largely free to design χ in a convenient way.

2.5. *Initial condition*

Because of our quasi-static assumption, the initial condition is prescribed by specifying initial values for the crack tip a^0 and the fluid front L^0, along with an initial profile for the fluid pressure $p^0(\Gamma_p)$. The pressure profile p^0 should be consistent with the boundary conditions of the fluid (Equations (11) and (12)). Once the pressure p^0 has been specified, the initial displacement $u^0(\mathcal{B})$ is computed by solving the static equilibrium equations in Section 2.1.

3. NUMERICAL ALGORITHM

We formulate the numerical algorithm by first discretizing in time, and then in space. This is an attractive approach because it allows the problem to be posed in a space-continuous (or semidiscrete) form at each time step. In this way, a different spatial discretization can be adopted later to find approximate solutions to the semidiscrete problem. This perspective is convenient when, for example, the crack becomes so long that the computational domain needs to be re-meshed to yield a good spatial discretization near the crack tip or when the block size s needs to be expanded to maintain a good approximation of the infinite domain.

3.1. *Time discretization*

The goal of the integration in time is to advance the solution variables from the current time t^n, to the next time t^{n+1}. We define the time step as $\Delta t^{n+1} \equiv t^{n+1} - t^n$.

The fluid front L and the crack tip a are advanced in time first because these variables define the domain over which the rest of the solution (u and p) is computed. We will only consider explicit schemes to advance L, because Equation (13) enables the direct evaluation of the fluid front velocity $\dot{L}$. In this article, we adopt a simple forward Euler scheme to advance L, namely,

$$L^{n+1} = L^n + \Delta t^{n+1}\frac{q^n}{2u_2^n}\bigg|_{x_1 - L^n} \tag{19}$$

Other schemes involving values at several previous times steps are also possible.

On the other hand, there is no direct way of obtaining the crack tip velocity $\dot{a}$, and therefore we simply make a guess as to where the crack tip a will be and then improve on this guess iteratively.

With the fluid front L^{n+1} determined and a guess for the crack tip a^{n+1} made, spaces of admissible displacement and pressure fields can be defined, namely,

$$\begin{aligned} S_u^{n+1} &= \left\{u = (u_1, u_2) \in \left[H^1(\mathcal{B}) \cap L^\infty(\mathcal{B})\right]^2 : u_2 = 0 \text{ on } \Gamma_b, u_1 = 0 \text{ on } \Gamma_\ell\right\}, \\ S_p^{n+1} &= \left\{p \in H^1\left(\Gamma_p\right) : p(L^{n+1}) = 0\right\} \end{aligned} \tag{20}$$

These are the spaces where we seek the semidiscrete solutions for the displacement $u^{n+1} \in S_u^{n+1}$ and the pressure $p^{n+1} \in S_p^{n+1}$ at time t^{n+1}.

To complete the time discretization, we also replaced the time derivative of the crack opening $\dot{u}_2$ in Equation (10) with a finite difference expression

$$v_2^{n+1} = \dot{u}_2\left(\Delta t^{n+1}, \Delta t^n, \ldots; u_2^{n+1}, u_2^n, u_2^{n-1}, \ldots\right) \tag{21}$$

which is possibly a function of the current and previous time steps and values of the crack opening. In this article, we adopt the simplest form for v_2^{n+1}, namely,

$$v_2^{n+1} = \frac{u_2^{n+1} - u_2^n}{\Delta t^{n+1}} \tag{22}$$

More accurate approximations are also possible. As evident in the next equation, by adopting approximations of Equation (21), the data at earlier time steps effectively act as known source terms.

The governing equations and natural boundary conditions for both the rock and the fluid in Sections 2.1 and 2.2 can be combined to produce the weak form of the problem. Its statement is as follows: find $(u^{n+1}, p^{n+1}) \in S_u^{n+1} \times S_p^{n+1}$ such that

$$\begin{aligned} &\int_{\mathcal{B}} w_{i,j} \mathbb{C}_{ijkl} u_{k,l}^{n+1}\, d\mathcal{B} + \int_{\Gamma_p} w_p\left(2v_2^{n+1}\right) d\Gamma + \frac{1}{\mu'} \int_{\Gamma_p} w_{p,1}\left(2u_2^{n+1}\right)^3 p_{,1}^{n+1}\, d\Gamma = \\ &-\sigma_0 \int_{\Gamma_t} w_2\, d\Gamma - \sigma_0 \int_{\Gamma_r} w_1\, d\Gamma + \int_{\Gamma_p} w_2 p^{n+1}\, d\Gamma + w_p(0)\frac{1}{2} Q_0 \end{aligned} \tag{23}$$

is satisfied for all admissible test functions $\left(w, w_p\right) \in S_u^{n+1} \times S_p^{n+1}$.

The solution of Equation (23) together with the values of the fluid front and crack tip positions enables then the computation of the SIF $(K')^{n+1}$ from Equation (15). The crack tip position a^{n+1} must be such that the crack propagation criterion (Equation (14)) is satisfied. If it is not, then an improved guess for the crack tip a^{n+1} is made based on the computed value of $(K')^{n+1}$, and the process is repeated in an iterative fashion until the propagation criterion is satisfied to within a chosen tolerance.

We summarize this entire algorithm in Algorithm 1.

Algorithm 1: Numerical algorithm for time advancement

Input: L^n, a^n, u^n, p^n
Output: $L^{n+1}, a^{n+1}, u^{n+1}, p^{n+1}$
Compute L^{n+1} explicitly by taking advantage of Equation (13)
Guess a^{n+1}
repeat
  Compute (u^{n+1}, p^{n+1}) from Equations (20), (21), and (23)
  Compute $(K')^{n+1}$ from Equation (15)
  If the crack propagation criterion (Equation (14)) is *not* satisfied, **then**
    Make improved guess for an $n+1$ on the basis of $(K')^{n+1}$
until *the crack propagation criterion (Equation (14)) is satisfied*

3.2. *Spatial discretization*

The semidiscrete problem in Equation (23) is still an infinite-dimensional one. To approximate its solution at each time step, we introduce a spatial discretization of the domain. In this article, we consider finite element meshes over $\mathcal{B}$ at each time step. In particular, because the domain $\mathcal{B}$ changes as the crack propagates, the mesh will slightly change as well. In the following, h denotes the largest diameter of an element in the mesh.

We then build finite element spaces $\left(S_u^h\right)^{n+1} \subset S_u^{n+1}$ and $\left(S_p^h\right)^{n+1} \subset S_p^{n+1}$ over the mesh at time t^{n+1} to approximate $u^{n+1}(\mathcal{B})$ and $p^{n+1}(\mathcal{B})$. The approximate solutions $u_h^{n+1} \in \left(S_u^h\right)^{n+1}$ and $p_h^{n+1} \in \left(S_p^h\right)^{n+1}$ are those that satisfy Equation (23) for all admissible test functions $\left(w, w_p\right) \in \left(S_u^h\right)^{n+1} \times \left(S_p^h\right)^{n+1}$, with Equation (21) evaluated instead as

$$v_2^{n+1} = \dot{u}_2\left(\Delta t^{n+1}, \Delta t^n, \ldots; \left(u_h^{n+1}\right)_2, \left(u_h^n\right)_2, \left(u_h^{n-1}\right)_2, \ldots\right) \tag{24}$$

and similarly for Equation (19). This problem leads to a system of nonlinear equations that can be solved using, for example, the Newton–Raphson method.

4. IMPLEMENTATION OF THE NUMERICAL ALGORITHM

A few additional choices need to be made to implement the algorithm in Section 3. First, we describe how we discretize the problem in space and time. Then we comment about the chosen strategies to advance the fluid front and the crack tip, which include the computation of SIF. We also detail the initialization of the Newton–Raphson iterations. Then finally, we specify the initial condition for the pressure profile used in all subsequent simulations.

4.1. Discretizations in space and time

Here we describe in detail the three types of approximations that must be made to solve the hydraulic fracture problem. First, we describe how to construct the spatial discretization over the computational domain. Then we outline the criteria we used for choosing the time step. And lastly, we discuss how we approximate the infinite medium with a finite block size.

4.1.1. Spatial discretization. The most interesting aspect of constructing spatial discretizations for the hydraulic fracture problem is that the domain of the fluid and the rock are changing in time. It is therefore necessary to devise efficient strategies to build the spaces $\left(S_u^h\right)^n$ and $\left(S_p^h\right)^n$ at each time step. Of course, this is much simpler in the context of this article because we are dealing with only a two-dimensional setting and an *a priori* known possible crack path.

We construct approximation spaces for the displacement field on a mesh of triangular elements over the domain of the rock $\mathcal{B}$. It is convenient, however, that each mesh over $\mathcal{B}$ defines a one-dimensional mesh of segments over the domain of the fluid Γ_p. In this way, this mesh of segments can be adopted to build approximation spaces for the pressures, the boundary condition (Equation (12)) is simple to impose, and integrations over Γ_p in Equation (23) involving pressure and displacement variables together can be more easily performed. In particular, meshing Γ_p requires a node to coincide with the fluid front location. In addition, it is convenient (although not necessary) for a node to coincide with the crack tip.

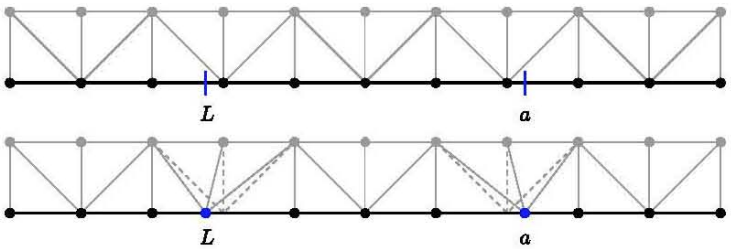

Figure 3. In the original mesh (top), the locations of the fronts L and a do not coincide with the nodes. In the modified mesh (bottom), the node closest to a moving front now coincides precisely with it (the dashed lines show the original mesh pattern).

The way we move the nodes is illustrated in Figure 3. Given a mesh over $\mathcal{B}$ at a certain time step, the idea is to move the node closest to the fluid front (or crack tip) to coincide with it. In this way, we can reuse essentially the same mesh at each time step, by temporarily moving two of its nodes to coincide with the fluid front and the crack tip. Because we have assumed that $L < a$, the two fronts will not share the same node as long as the mesh size is small enough. We monitored this assumption in all the simulations in this article.

With the mesh at time t^{n+1} built, we construct $\left(S_u^h\right)^{n+1}$ as the set of continuous two-dimensional vector fields that are affine when restricted to each element over $\mathcal{B}$, known as $[P_1]^2$ elements in the finite element literature (or piecewise linear triangular elements). When these functions are evaluated over Γ_p, they define continuous displacement fields that are affine over each segment of Γ_p. For the pressure field, we made a similar choice, namely, we set $\left(S_p^h\right)^{n+1}$ to be the space of continuous functions over Γ_p that are affine over each segment (also known as piecewise linear one-dimensional elements). We should note that each node in the mesh is associated with two unknowns for the displacement field (one for each component), and nodes on Γ_p contain one more unknown, which is the value of the pressure.

Another challenge arising in the spatial discretization is that to obtain more accurate solutions, it is necessary to represent the singularity at the crack tip as well as the steep pressure gradient at the fluid front as the fluid lag vanishes (when $L/a \to 1$). In this article, we do this by using finer elements closer to the crack and coarser elements farther away from the crack. This is particularly important for the crack tip singularity because the convergence of the solution with the mesh size could be rather slow otherwise ($\sim h^{1/2}$ for the stresses). A useful alternative, which we have tested, is to include the crack tip singularities as enrichment shape functions, as in [34, 35, 27]. Such an approach can recover an optimal order of convergence ($\sim h$ for stresses) and enables the use of less refined meshes near the cracktip. Of course, it does not help with steep pressure gradients when $L \sim a$. Despite the benefits of such an approach, its proper description is rather laborious, so we decided against it in this manuscript.

4.1.2. Time step selection. The selection of the time step size was mainly based on accuracy and practical considerations, and *not* on stability. We have not systematically explored the stability properties of the method. Nevertheless, we highlight that we did not find a numerically unstable solution in any of the numerical experiments we conducted. In fact, the method seems to be quite robust with respect to the selection of the time step.

The main consideration that guided our selection of the time step was controlling the growth of the crack length. More specifically, we selected the time step so that $\Delta a/a$ never exceeded a desired value (for the simulations in Section 5, we had $\Delta a/a < 0.25$). There were two reasons behind this choice. First, as we show in Section 5, we selected meshes that are very refined near the crack tip. Therefore, by limiting the growth of the crack length, we could guarantee that the crack did not step into a region with a coarser mesh. Second, in iterating to find the location of the crack tip at each time step, it is necessary to compute the value of the SIF for different possible locations of the crack tip (see Section 2.4 and Section 4.3). By limiting the crack growth, it is possible to reuse much of the information in all iterations for each time step.

We have found that we can limit the value of $\Delta a/a$ at each time step if the time step size is proportional to the elapsed time (i.e. $\Delta t \sim t$). In this article, after each decade of time elapses, we increase Δt by a factor of ten. We should note that choosing $\Delta t \sim t$ may lead to large inaccuracy of the solution when $L \sim a$ (this is mostly due to the explicit time advancement of L). Hence, when we have $L/a > 0.9$, we stop increasing Δt and keep it constant as time t continues to increase.

4.1.3. Infinite medium approximation. In addition to the time and spatial discretizations, the third critical numerical approximation we make is to use a domain of a finite size, specifically, a square block of edge size s. From the subsequent numerical examples, we observed that most of the numerical error stems from this last approximation.

In Appendix A, we show through a numerical experiment that the error arising from the finite block size scales as s^{-2}. Thus, reducing the error caused by the finite block size is the first issue to address to

improve the accuracy of the method. This could likely be accomplished by adopting one of several alternative remedies, such as imposing boundary conditions based on Dirichlet-to-Neumann maps [36], adopting special "infinite elements" along the outer boundaries $\Gamma_t \cup \Gamma_r$ of the computational domain [37], or simply using boundary elements for the external region.

4.2. *Fluid front advancement*

As described in Section 3, advancing the fluid front in time requires the computation of the flow rate at the fluid front $q(L)$, see Equations (13) or (19). The computation of fluxes across surfaces in the finite element setting is more accurately performed using domain integrals rather than surface ones [38]. Hence, instead of evaluating $q(L)$ directly through its definition in Equation (10), we compute

$$q(L) = -\int_{\Gamma_p} w_p (2v_2) d\Gamma - \frac{1}{\mu'} \int_{\Gamma_p} w_{p,1} (2u_2)^3 p_{,1} d\Gamma \tag{25}$$

where w_p is a smooth enough function that satisfies $w_p(0) = 0$ and $w_p(L) = 1$. To compute $q^n(L)$, we set $v_2 = v_2^n, p = p_h^n, u_2 = \left(u_h^n\right)_2$, and $w_p = N_L$ in Equation (25), where N_L is the shape function of the pressure associated with the node at the fluid front $x_1 = L$. For the types of finite element spaces considered here, this means that at the fluid front we have $N_L(L) = 1$, whereas all other shape functions in $\left(S_p^h\right)^{n+1}$ are equal to zero there. In addition, because N_L is nonzero only in the element that has the fluid front as a node, the integral in Equation (25) only needs to be computed over that single element.

4.3. *Computation of the stress intensity factor*

Similar reasons to those mentioned in the last section lie behind the computation of the SIF K' with a domain integral (as described in Section 2.4) instead of a contour integral like the J-integral. In this section, we describe our selection of χ to use in Equations (16) and (17), which is analogous to the choice of w_p in Equation (25).

The continuous scalar field χ over $\mathcal{B}$ should satisfy $\chi = 0$ on the boundary $\Gamma_\ell \cup \Gamma_t \cup \Gamma_r$, and $\chi = 1$ at the crack tip $(a, 0)$. To construct χ, we consider a (closed) circle $\mathcal{C}_\chi$ of radius r_χ centered at the crack tip (see Figure 4). Elements whose interior lies outside $\mathcal{C}_\chi$ have a constant value of $\chi = 0$ within the element, whereas elements that lie completely inside $\mathcal{C}_\chi$ have a constant value of $\chi = 1$ within the element. Elements whose interior intersects the circumference $\partial\mathcal{C}_\chi$ have χ defined as an affine function, taking the value $\chi = 0$ at the nodes outside $\mathcal{C}_\chi$, and the value $\chi = 1$ at the nodes in $\mathcal{C}_\chi$.

In this way, χ is a continuous function with derivatives devoid of singularities. This, together with the fact that that the gradient of χ is only nonzero in the ring of elements whose interior intersect $\partial\mathcal{C}_\chi$, makes its use in computing K' from Equation (15) very simple and efficient. In fact, computing I_u in Equation (16) only needs integrals over this ring of elements. The computation of I_p in Equation (17) involves integrals over the elements in the mesh of the fluid domain Γ_p over which χ is different than zero (i.e. those elements in Γ_p that intersect $\mathcal{C}_\chi$).

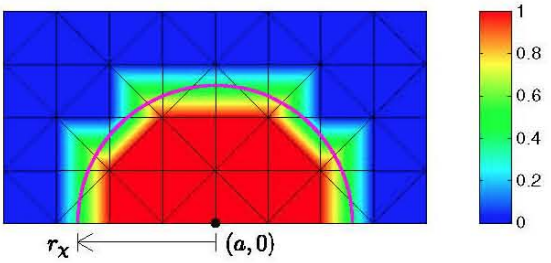

Figure 4. The scalar field χ over the domain $\mathcal{B}$.

A couple of remarks about this choice of χ are appropriate. First, although the value of $I_u + I_p$ is independent of the choice of χ for the exact solution u of the problem, it is not when u is replaced by its numerical approximation u_h. Rather, the dependence of the computed value of $I_u + I_p$ on the choice of χ will progressively decrease with the mesh size. Second, by constructing χ in a way that its gradient grows as h decreases, the convergence rate of the computed value of K' with h is not optimal. It could be improved by selecting a function χ that does not change with the mesh size, among others. In our case, this was unnecessary because the values we obtained were quite accurate in view of the error introduced by the infinite medium approximation, as discussed earlier in Section 4.1.3.

4.4. Crack tip advancement

As mentioned in Section 3, there is no explicit expression for the crack tip velocity. So the crack tip location at t^{n+1} must be found by making a guess and then improving on that guess in iterative fashion. We describe this procedure as follows. We want to increase the crack tip position by an unknown amount $\Delta a^{n+1} = a^{n+1} - a^n$ such that the crack propagation criterion (Equation (14)) is satisfied at time t^{n+1}.

To find Δa^{n+1}, we adopted a root-finding method that has guaranteed convergence at a relatively fast rate [39, 40]. It is a Regula Falsi method (false position) and requires two initial guesses for the crack tip increment that bracket the root of the equation we wish to solve. We denote the first initial guess with an asterisk (*), which should yield $K' > K'_c$. In addition, we denote the second initial guess with two asterisks (**), which should yield the opposite, $K' < K'_c$. In this article, we choose

$$\left(\Delta a^{n+1}\right)^* = 0 \tag{26}$$

for the first initial guess, which indicates a guess of no crack propagation. If this guess yields $K' < K'_c$, then we conclude that no crack propagation occurs, and we do not have to iterate further. However, if this guess yields $K' > K'_c$, then crack propagation does occur, and we choose

$$\left(\Delta a^{n+1}\right)^{**} = \left(\frac{\Delta a^n}{\Delta t^n}\right)\Delta t^{n+1} \tag{27}$$

for the second initial guess. In general, this guess will bracket the root if the rate of crack propagation decreases with time (which is the case for all the simulations shown in this article).

There are two special cases to be considered, for which Equations (26) and (27) might fail to return valid initial guesses. One special case appears when $\Delta a^n = 0$, that is, when the crack tip did not advance at time t^n. In this case we adopted the alternative

$$\left(\Delta a^{n+1}\right)^{**} = \dot{L}^{n+1}\Delta t^{n+1} \tag{28}$$

which is the distance that the fluid front traveled during this time step and is partially rooted in the observation that often the fluid front and crack tip velocities are very similar. If this guess does not yield $K' < K'_c$, we successively double $\left(\Delta a^{n+1}\right)^{**}$ until it does.

One other special case is when the fluid front exceeds the guess for the crack length. This might occur, for example, during the first initial guess when using a large time step Δt^{n+1}. Hence, if we have $L^{n+1} > a^n$, we instead choose

$$\left(\Delta a^{n+1}\right)^* = \left(L^{n+1} + h\right) - a^n \tag{29}$$

for the first initial guess, where h is the element size of the mesh in that region. In other words, we ensure that we have $L < a$ by always keeping a minimum distance of h between the fluid front and the crack tip.

As with most nonlinear equation solvers, the strategy outlined earlier is not completely robust, namely, the initial guesses might not be good ones, either because they do not bracket a root or

because they bracket too many roots. In the examples in this article, however, this strategy has worked remarkably well.

4.5. *Newton–Raphson initial guess*

For each guess of the crack tip position, it is necessary to solve Equation (23) for the coupled elastic and pressure fields, as detailed in Section 3.2. We solve it using the Newton–Raphson method, which requires a good initial guess. We denote the initial guess for the unknown values at time t^{n+1} with an asterisk (*).

Because the nonlinearity arises from the fluid equations, an initial guess is only required for the crack opening $u_2^{n+1}(x_1)$ and pressure $p^{n+1}(x_1)$ in the domain of the fluid Γ_p (note that $x_2 = 0$ in this domain). The initial guess we use is

$$\begin{aligned} \left(u_2^{n+1}\right)^*(x_1) &= u_2^n\left(x_1 \frac{a^n}{a^{n+1}}\right), \\ \left(p^{n+1}\right)^*(x_1) &= p^n\left(x_1 \frac{L^n}{L^{n+1}}\right) \end{aligned} \tag{30}$$

where we have the known functions $u_2^n(x_1)$ and $p^n(x_1)$ from the previous time step. This guess is basically a "stretching" of the profiles at t^n to match the new domains at t^{n+1}. This strategy has led to convergence of the Newton–Raphson iterations for all the simulations described in this article.

4.6. *Initial condition*

We have observed that the long-time evolution of the system is not especially sensitive to the initial condition, and therefore we have some liberty in constructing an initial condition. We choose the initial crack length a^0 and the initial fluid front L^0 with $L^0 < a^0$. We prescribe the pressure profile $p^0(\Gamma_p)$ to vary linearly from $\hat{p}$ at the fluid inlet to zero at the fluid front, namely,

$$p^0 = \hat{p}\left(1 - \frac{x_1}{L^0}\right) \tag{31}$$

With the pressure p^0 and the geometry specified, the initial displacement $u^0(\mathcal{B})$ is computed as the solution of the linear elastostatics equations in Section 2.1. More precisely, we find $u^0 \in S_u^0$ such that Equation (23) is satisfied for all test functions $w \in S_u^0$ with $w_p = 0$.

It remains to compute $\hat{p}$ such that the inlet boundary condition (Equation (11)) is satisfied. Taking advantage of the ability to superimpose solutions of the linear elasostatics equations, the displacement field can be constructed as

$$u^0 = u^\sigma + u^* \frac{\hat{p}}{\hat{p}^*} \tag{32}$$

for any value of $\hat{p}$. The displacement field $u^*(\mathcal{B})$ is computed for an arbitrary nonzero value of the inlet pressure $\hat{p} = \hat{p}^*$ with no far-field stress (i.e. setting $\sigma_0 = 0$). The displacement field $u^\sigma(\mathcal{B})$ is the response due solely to the far-field stress, so the pressure is set to zero, $\hat{p} = 0$. With the two computations made to find u^σ and u^*, the correct value for $\hat{p}$ can be found by solving the nonlinear scalar equation

$$\hat{q}^*\left(\frac{u_2^\sigma(0)}{u_2^*(0)} + \frac{\hat{p}}{\hat{p}^*}\right)^3 \left(\frac{\hat{p}}{\hat{p}^*}\right) - \frac{1}{2}Q_0 = 0 \tag{33}$$

where $\hat{q}^*$ is the flow rate corresponding to $\hat{p} = \hat{p}^*$, which is computed as

$$\hat{q}^* = \frac{1}{\mu'}\left(2u_2^*\right)^3 \frac{\hat{p}^*}{L^0} \tag{34}$$

It is simple to see that the fourth-order polynomial in Equation (33) has a single positive root because it is negative at $\hat{p} = 0$ and its derivative is nondecreasing.

A good initial guess for solving Equation (33) is

$$\hat{p} = \hat{p}^* \left(\frac{\frac{1}{2} Q_0}{\hat{q}^*} \right)^{1/4} \tag{35}$$

5. NUMERICAL EXAMPLES

In this section, we perform sample simulations using the algorithm outlined in this article and compare the results with two known similarity solutions. One of these similarity solutions occurs when the crack propagates under zero far-field stress [5], and the other occurs for late times for any nonzero value of the far-field stress [4].

When displaying the simulation results, we will normalize the solution variables by their corresponding characteristic dimensions (which will be defined later for each problem). We will define characteristic dimensions for the position a_c, time t_c, displacement δ, and pressure p_c.

To compare the simulation results with the similarity solutions, we need to introduce similarity variables for the position ξ and time τ, which we define as follows:

$$\xi = \frac{x_1}{a}, \quad \tau = \frac{V_0}{a_c \delta} + \frac{t}{t_c} \tag{36}$$

The position ξ takes on values of $0 < \xi < 1$ in the crack domain. The time τ is corrected for the amount of fluid volume V_0 already injected into the crack at zero time. The volume is obtained by integrating the opening profile over the fluid domain Γ_p as follows:

$$V_0 = 2 \int_{\Gamma_p} 2 u_2 d\Gamma \Big|_{t=0} \tag{37}$$

We also introduce similarity variables for the crack length γ, pressure Π, and crack opening Ω by scaling with the appropriate powers of τ as dictated by the similarity solution:

$$\gamma = \left(\frac{a}{a_c} \right) \tau^{-2/3}, \quad \Pi = \left(\frac{p}{p_c} - \sigma_0^* \right) \tau^{1/3}, \quad \Omega = \left(\frac{2 u_2}{\delta} \right) \tau^{-1/3} \tag{38}$$

The previous equations can be used to describe both similarity solutions, if we use $\sigma_0^* = 0$ for the zero far-field stress solution, and $\sigma_0^* = 1$ for the late-time solution. We note that the similarity solutions are governed solely by the dimensionless toughness K_c^*, which is defined through a combination of the physical parameters of the problem:

$$K_c^* = \frac{K_c'}{\left(\mu' Q_0 E'^3 \right)^{1/4}} \tag{39}$$

So for each value of K_c^*, there is a corresponding value of γ, and corresponding functions $\Pi(\xi)$ and $\Omega(\xi)$, which have no dependence on τ.

In the following, we carry out simulations for two different cases (zero far-field stress and late time) and discuss the results. Then after that, we provide details about the type of mesh used, the time step selection, the block size, and performance.

5.1. *Zero far-field stress solution*

It was shown by Garagash [5] that a similarity solution could be found when the far-field stress is zero. In this solution, the fluid fraction L/a is a constant and its size depends only on K_c^*. For increasing values of K_c^*, the fluid fraction increases and eventually approaches $L/a \to 1$. For $K_c^* > 1.6$, the size of the fluid fraction is greater than 0.99, and thus nearly fills the entire crack length.

Although the similarity solution is exact only when the far-field stress is zero, it is still reasonably accurate for nonzero values of σ_0 if

$$\sigma_0 \left(\frac{t}{\mu' E'^2} \right)^{1/3} \ll 1 \tag{40}$$

Notice that this inequality is also valid when time t is small. Thus, the similarity solution can alternatively be interpreted as an "early-time" solution for nonzero far-field stress.

For the simulations in this section, we define the characteristic dimensions that normalize the solution variables as

$$a_c = a^0, \quad t_c = \left(\frac{\mu' (a^0)^6}{Q_0^3 E'} \right)^{1/4}, \quad \delta = \left(\frac{\mu' Q_0 (a^0)^2}{E'} \right)^{1/4}, \quad p_c = \left(\frac{\mu' Q_0 E'^3}{(a^0)^2} \right)^{1/4} \tag{41}$$

We have performed a simulation with $\sigma_0 = 0$ and have compared it with the known similarity solution. We chose the dimensionless toughness to be $K_c^* = 0.6$, which is small enough to allow a significant fluid lag. The initial fluid fraction was $L^0/a^0 = 1/4$, and we advanced the simulation for a total time of $t/t_c = 1.6$.

In Figure 5, we show the time evolution of the fluid front, crack tip, and inlet pressure, along with snapshots of the pressure and opening profiles. We observe that the crack starts propagating at

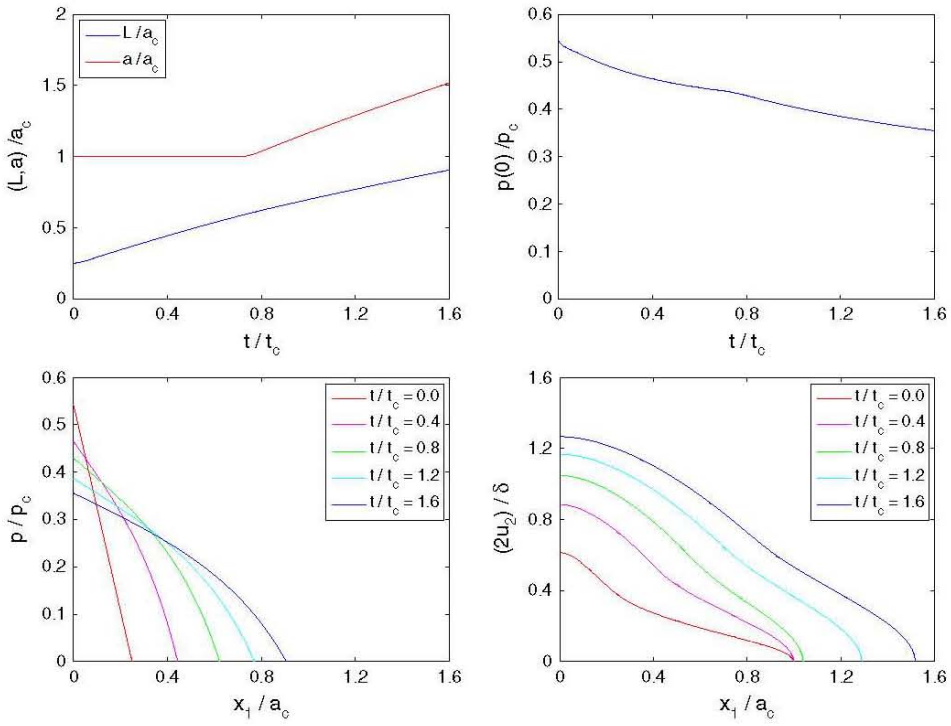

Figure 5. Time evolution of the fluid front and crack tip (top-left) and inlet pressure (top-right). Profiles for the pressure (bottom-left) and opening (bottom-right).

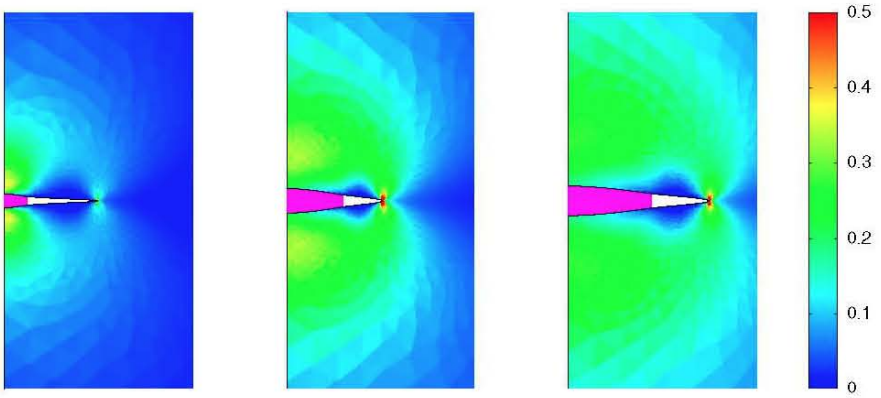

Figure 6. Snapshots of the rock with the injected fluid. From left to right, the times are $t/t_c = 0.0$, $t/t_c = 0.8$, and $t/t_c = 1.6$. The color in the rock corresponds to the von Mises stress normalized by the plane-strain modulus, σ_v/E'. The displacement is magnified by a factor of $(0.25)(a_c/\delta)$. Note that only the region of the computational domain in the neighborhood of the crack is shown.

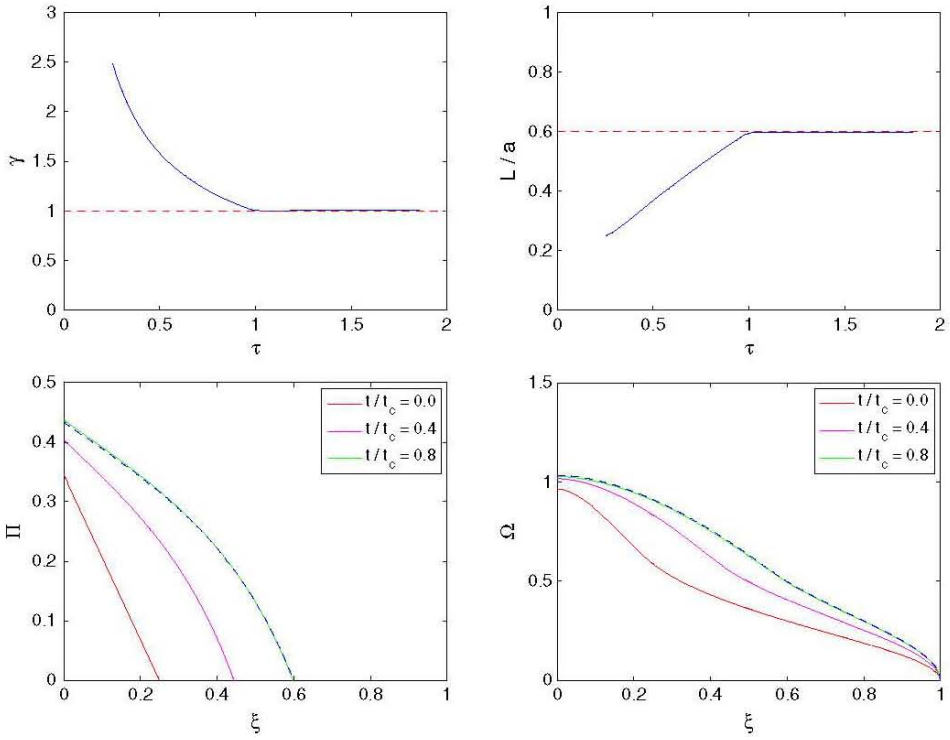

Figure 7. Time evolution of the similarity crack length (top-left) and fluid fraction (top-right). Profiles for the similarity pressure (bottom-left) and opening (bottom-right). Note that we do not show the profiles at times $t/t_c = 1.2$ and $t/t_c = 1.6$ because they are the same within plotting accuracy to the profiles at $t/t_c = 0.8$. The dashed lines correspond to the zero far-field stress similarity solution.

about $t/t_c = 0.7$. The inlet pressure $p(0)$ steadily decreases throughout the simulation. The crack opening is always increasing at fixed values of the spatial coordinate x_1. In Figure 6, we show snapshots of the displacement of the rock with the injected fluid.

To compare the simulation results with the similarity solution, we computed the similarity variables using Equation (38) with $\sigma_0^* = 0$. In Figure 7, we show the time evolution of the similarity crack length

γ and fluid fraction L/a, along with profiles of the similarity pressure Π and opening Ω at several snapshots in time. We observe that there is agreement with the similarity solution as soon as the crack starts propagating.

We have performed a few more simulations like the one just described, but with different values for the dimensionless toughness K_c^*. In Table I, we show the values of the dimensionless variables γ, L/a, $\Pi(0)$, and $\Omega(0)$ at the end of the simulation when $t/t_c = 1.6$. We compute the "exact" values for the similarity solution using the numerical method presented by Garagash with 50 elements [5]. We observe that there is good agreement between the simulation results and the similarity solution, and this provides verification of our method.

5.2. *Late-time solution*

It was shown by Spence and Sharp [4] that a similarity solution can be found in the late-time limit when the far-field stress is nonzero. In this solution, the fluid lag is assumed to be negligible, and therefore we have $L/a \cong 1$. It was shown in numerical simulations by Lecampion [6] that this is a valid assumption at times of the order of

$$t_c = \frac{\mu' E'^2}{\sigma_0^3} \tag{42}$$

or larger. Notice that as $\sigma_0 \to 0$, we have $t_c \to \infty$, and hence the simulation never evolves into the late-time regime. This is consistent with what was observed in Section 5.1, where the zero far-field stress similarity solution was interpreted as an early-time solution that kept the fluid fraction constant, and hence the fluid never evolved to fill the entire crack.

For the simulations in this section, we define the characteristic dimensions that normalize the solution variables as

$$a_c = \left(\frac{\mu' Q_0 E'^3}{\sigma_0^4}\right)^{1/2}, \quad \delta = \left(\frac{\mu' Q_0 E'}{\sigma_0^2}\right)^{1/2}, \quad p_c = \sigma_0 \tag{43}$$

together with the definition of t_c in Equation (42).

We have performed a simulation in which we compared the numerical solution against the late-time similarity solution. We chose the dimensionless toughness to be $K_c^* = 0.5$, which is small enough to allow a significant fluid lag at early time. The initial crack length was $a^0/a_c = 1/512$, and the initial fluid fraction was $L^0/a^0 = 1/2$. We advanced the simulation for a total time of $t/t_c = 2.5$.

In Figure 8, we show the time evolution of the fluid front, crack tip, and inlet pressure. In Figure 9, we show snapshots of the pressure and opening profiles. We observed that the crack starts propagating at about $t/t_c = 4 \times 10^{-5}$. The inlet pressure $p(0)$ steadily decreases throughout the simulation. The crack opening is always increasing at fixed values of the spatial coordinate x_1. At late time, the pressure gradient is small throughout most of the fluid region, except near the fluid front where it is very large.

To compare the simulation results with the similarity solution, we computed the similarity variables using Equation (38) with $\sigma_0^* = 1$. In Figure 10, we show the time evolution of the similarity crack length γ and fluid fraction L/a, along with profiles of the similarity pressure Π and opening Ω at

Table I. Similarity variables at $t/t_c = 1.6$.

K_c^*	γ		L/a		$\Pi(0)$		$\Omega(0)$	
	Exact	Numerical	Exact	Numerical	Exact	Numerical	Exact	Numerical
0.4	1.4919	1.4974	0.3950	0.3926	0.3883	0.3910	1.0210	1.0167
0.5	1.1866	1.1915	0.5025	0.4990	0.4123	0.4141	1.0262	1.0218
0.6	1.0024	1.0058	0.5997	0.5962	0.4337	0.4359	1.0339	1.0294
0.7	0.8822	0.8842	0.6849	0.6819	0.4529	0.4555	1.0436	1.0390
0.8	0.7995	0.8007	0.7574	0.7555	0.4704	0.4732	1.0549	1.0500

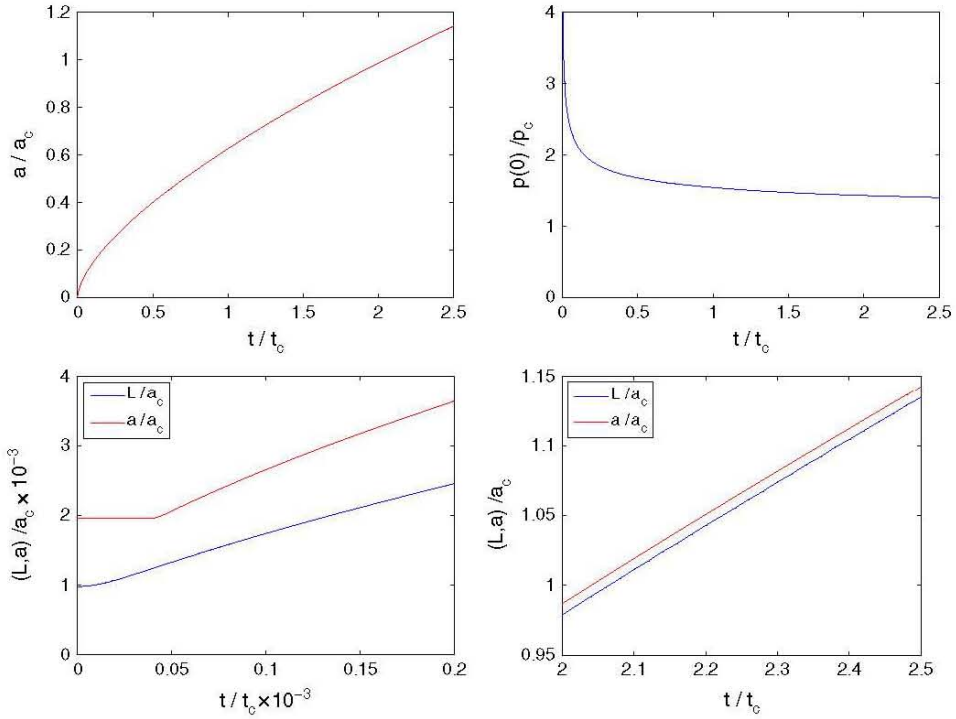

Figure 8. Time evolution of the crack tip (top-left) and inlet pressure (top-right). Zoom of the fluid front and crack tip at early time (bottom-left) and late time (bottom-right).

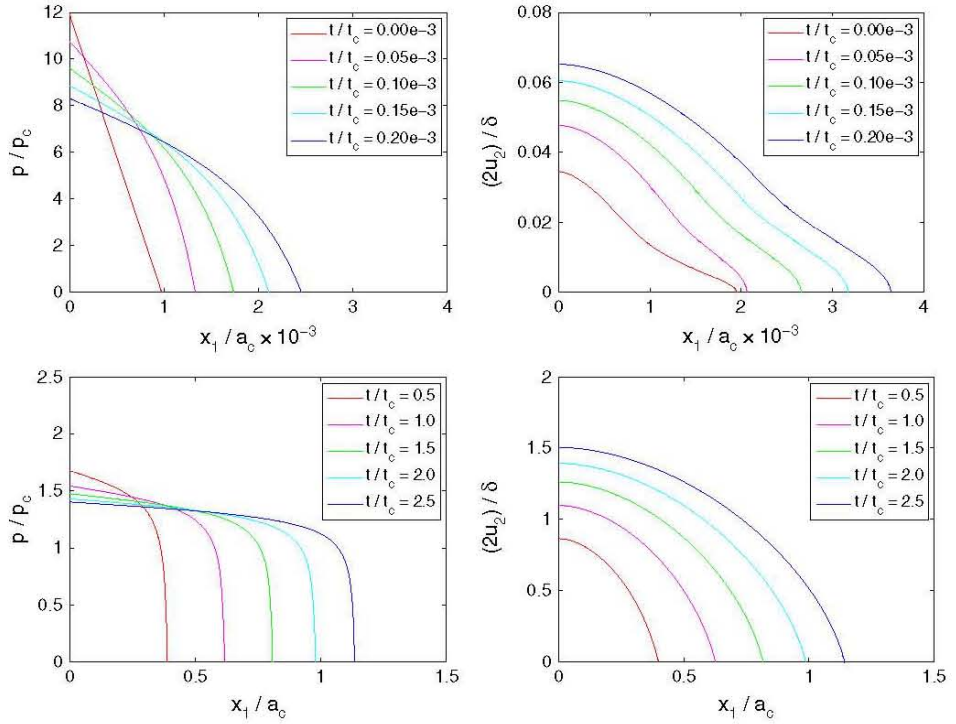

Figure 9. Early-time profiles for the pressure (top-right) and opening (top-right). Late-time profiles for the pressure (bottom-left) and opening (bottom-right).

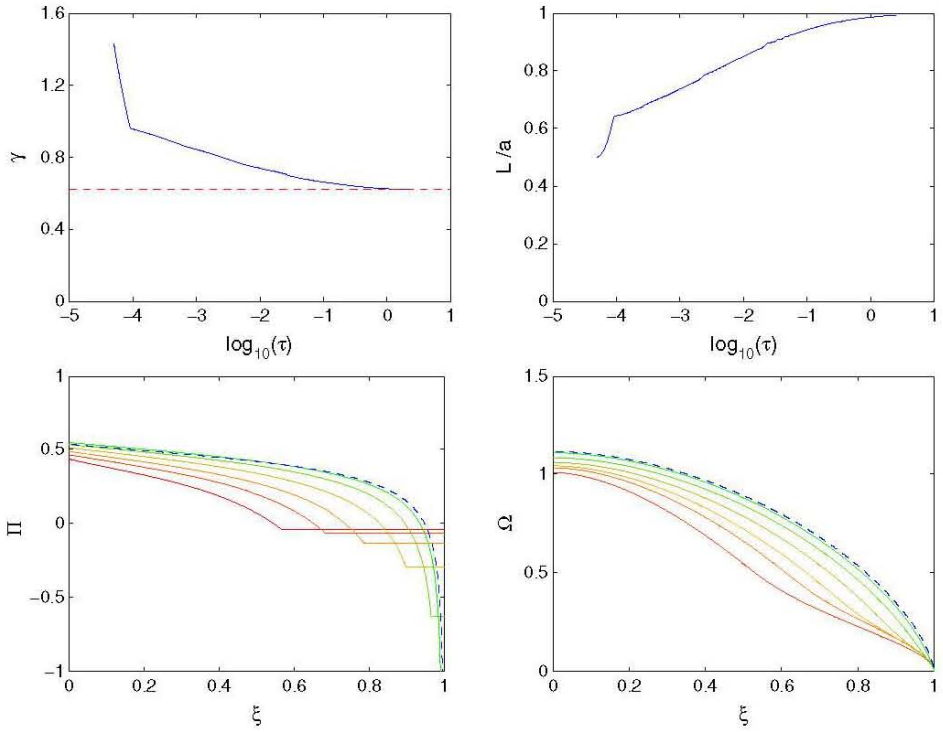

Figure 10. Time evolution of the similarity crack length (top-left) and fluid fraction (top-right). Profiles for the similarity pressure (bottom-left) and opening (bottom-right). Dashed lines correspond to the late-time similarity solution. We show the pressure and opening profiles at times $t/t_c = (2.5)10^{n-6}$ for values of $n = 1$ (red) through $n = 6$ (green).

several snapshots in time. We observe that as τ becomes large, the similarity variables computed from the simulation asymptotically approach the values predicted by the similarity solution. In addition, as τ grows the fluid fraction evolves toward $L/a \to 1$, which is a necessary condition for the late-time similarity solution to be valid. The agreement between the simulation results and the similarity solution provides further verification of the method.

5.3. Discretizations and performance

All simulations in this article were performed with the mesh shown in Figure 11. This mesh contains 14,056 elements. It has a highly refined region in the neighborhood of the crack with an element size of $h/s = 1/8192$. However, along the top and right sides, the element size is coarser, with $h/s = 1/8$.

As the crack grows, the block size s needs to be increased to keep the crack in the highly refined mesh region, and also to keep the infinite medium approximation valid. When re-meshing, it is not

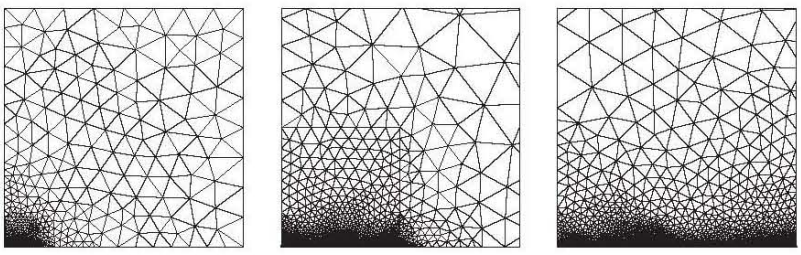

Figure 11. Mesh used for the simulations in the article (left). The mesh is highly refined near in the crack region. We also show an enlarged view of the bottom-left corner at 4× magnification (middle) and at 16× magnification (right).

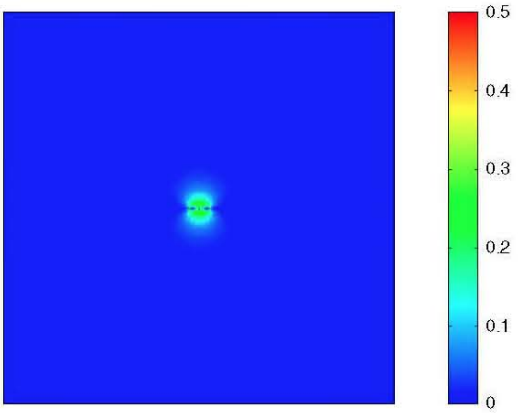

Figure 12. Snapshot of the entire domain of the problem at the final time $t/t_c = 1.6$ for the simulation in Section 5.1. The computational domain $\mathcal{B}$ comprises the upper-right corner of the block, and the other three corners are reproduced by symmetry. The color in the rock corresponds to the von Mises stress normalized by the plane-strain modulus, σ_v/E'. For an enlarged view near the crack, see the rightmost snapshot in Figure 6.

necessary to create an entirely new mesh but rather to just rescale the coordinates of the current mesh. In this article, when the crack size exceeded $a/s > 1/16$, we doubled the size of the block. In this way, the inequality $1/32 < a/s < 1/16$ was always satisfied. In Figure 12, we show the entire computational domain at the final time for the simulation in Section 5.1.

The simulation in Section 5.1 was performed with 64 time steps of equal size and took approximately 50 min to complete. When the crack was propagating, approximately three or four iterations were needed to find the crack tip location. This means that the time steps involving crack propagation took approximately three to four times longer to compute than those that did not. For each crack tip iteration, two or three Newton–Raphson iterations were needed to solve the nonlinear system of equations.

The simulation in Section 5.2 was performed with 264 time steps and took approximately 455 min to complete. As mentioned in Section 4.1.2, the size of the time step was increased periodically throughout the simulation, so that smaller time steps were used when the crack was small and larger time steps were used when the crack was large. Early in the simulation, approximately three or four iterations were needed to find the crack tip location when the crack was propagating, but later in the simulation approximately seven or eight iterations were needed. For each crack tip iteration, usually just three Newton–Raphson iterations were needed to solve the nonlinear system of equations regardless of whether it was early or late in the simulation.

The simulations described in this article were implemented in C++ and ran on a 3-GHz Intel Xeon CPU with 1 MB of cache memory and 2 GB of RAM.

6. CONCLUSIONS

In this article, we have created a finite-element-based algorithm to simulate the hydraulic fracture problem. The algorithm is capable of handling the nonlinear coupling between the fluid pressure and the crack opening, and is able to allow the existence of a fluid lag. The agreement of our simulations with two known similarity solutions provides verification of our algorithm.

An interesting observation that arose from the numerical experiments was that the major contribution to the error in the solution was from the infinite domain approximation. Another interesting observation is that solving for the position of the crack tip at each time step was very robust. For accurate solutions, we adopted highly refined meshes near the crack tip. We did this to capture both the stress singularity that occurs there and also the steep pressure gradient that arises

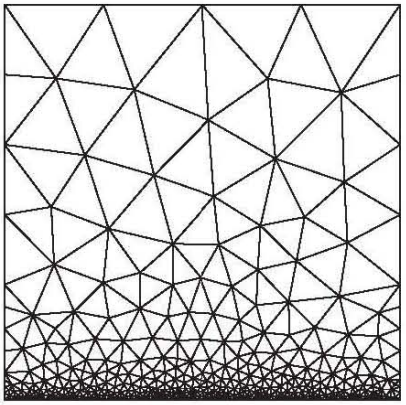

Figure 13. A mesh that has refinement along the entire bottom of the block.

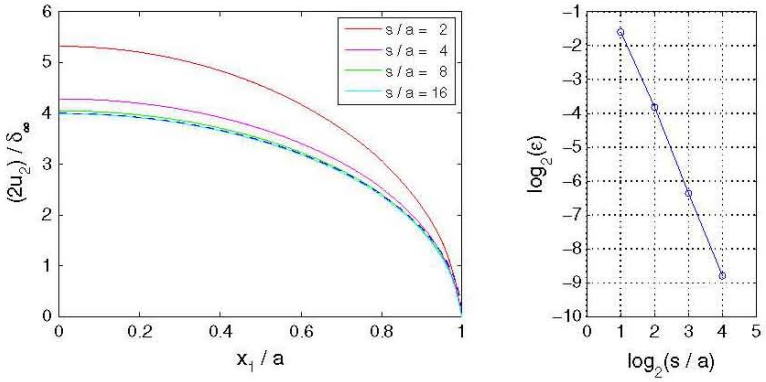

Figure 14. Opening profiles for increasing block sizes, with the dashed line representing the analytical solution for the infinite medium (left). Also, a convergence curve for the error in the opening at the inlet (right).

when the fluid lag vanishes. Using enrichments in the finite element spaces to capture these phenomena will likely allow the use of coarser meshes for the same accuracy.

Although we restricted the application of the algorithm in this article to a relatively simple hydraulic fracture problem, the algorithm can be easily extended to consider several other cases of interest. For example, it could be used to model the phenomenon of leak-off or fracturing fluids with non-Newtonian rheology.

APPENDIX A: INFINITE MEDIUM APPROXIMATION

In this section, we numerically explore the minimum block size needed to obtain an infinite medium approximation of a prescribed accuracy. To simplify the analysis, we will prescribe a constant pressure p along the entire length of the crack face, so that $L=a$ and the lag region vanishes (i.e. $\Gamma_v=\varnothing$). Because we are prescribing the pressure, it is not necessary to solve the fluid equations, and thus this problem is a standard elastostatics problem. When the elastic medium is infinite, and the pressure along the crack face is constant, there is a known analytical expression for the opening profile

$$\frac{2u_2}{\delta_\infty} = 4\left(\frac{p}{\sigma_0} - 1\right)\sqrt{1-\left(\frac{x_1}{a}\right)^2} \tag{A1}$$

where the characteristic displacement is defined as

$$\delta_\infty = \frac{\sigma_0 a}{E'} \tag{A2}$$

We chose the constant pressure to be $p/\sigma_0 = 2$ and computed the opening profile using different block sizes. An example of the type of mesh we used is shown in Figure 13. The element size along the bottom edge was set to $h/a = 1/64$ and those on the top edge to $h/a = 1/2$ for all block sizes. This means that the bigger blocks necessarily contained more elements.

As we increase the size of the block, the opening profile should converge to that of the infinite medium. We computed the error in the opening profile by comparing its value at the inlet to the analytical solution, namely,

$$\varepsilon = \left| 1 - \frac{u_2^s(0)}{u_2(0)} \right| \tag{A3}$$

where we use the superscript s to denote the inlet opening computed with the finite block size, and we use no superscript to denote the analytical solution.

In Figure 14, we show the opening profile for increasing values of the block size s/a, along with the corresponding values of ε in log scale. We see that the slope of the convergence curve is approximately -2, and the opening profile is converged to within plotting accuracy for $s/a = 16$. As described in Section 5.3, this is the minimum ratio we adopted for the simulations in Section 5.

ACKNOWLEDGEMENTS

This study was supported by the Office of Naval Research Young Investigator Award, under contract/grant number: N000140810852 and National Science Foundation Career Award, under contract/grant number: CMMI-0747089.

REFERENCES

1. Rubin AM. Propagation of magma-filled cracks. *Annual Review of Earth and Planetary Sciences* 1995; **23**:287–336.
2. Simoni L, Secchi S. Cohesive fracture mechanics for a multi-phase porous medium. *Engineering Computations* 2003; **20**:675–698.
3. Adachi J, Siebrits E, Peirce A, Desroches J. Computer simulation of hydraulic fractures. *International Journal of Rock Mechanics and Mining Sciences* 2007; **44**:739–757.
4. Spence DA, Sharp P. Self-similar solutions for elastohydrodynamic cavity flow. *Proceedings of the Royal Society of London A* 1985; **400**:289–313.
5. Garagash DI. Propagation of a plane-strain hydraulic fracture with a fluid lag: Early-time solution. *International Journal of Solids and Structures* 2006; **43**:5811–5835.
6. Lecampion B, Detournay E. An implicit algorithm for the propagation of a hydraulic fracture with a fluid lag. *Computer Methods in Applied Mechanics and Engineering* 2007; **196**:4863–4880.
7. Khristianovic SA, Zheltov YP. Formation of vertical fractures by means of highly viscous liquid. *Fourth World Petroleum Congress Proceedings*, 1955; 579–586.
8. Geertsma J, de Klerk F. A rapid method of predicting width and extent of hydraulically induced fractures. *Journal of Petroleum Technology* 1969; **21**:1571–1581.
9. Desroches J, Detournay E, Lenoach B, Papanastasiou P, Pearson JRA, Thiercelin M, Cheng A. The crack tip region in hydraulic fracturing. *Proceedings: Mathematical and Physical Sciences* 1994; **447**:39–48.
10. Detournay E. Propagation regimes of fluid-driven fractures in impermeable rocks. *International Journal of Geomechanics* 2004; **4**:35–45.
11. Garagash D, Detournay E. The tip region of a fluid-driven fracture in an elastic medium. *Journal of Applied Mechanics* 2000; **67**:183–192.
12. Adachi JI, Detournay E. Self-similar solution of a plane-strain fracture driven by a power-law fluid. *International Journal for Numerical and Analytical Methods in Geomechanics* 2002; **26**:579—604.
13. Garagash DI, Detournay E. Plane-strain propagation of a fluid-driven fracture: Small toughness solution. *Journal of Applied Mechanics* 2005; **72**:916–928.
14. Garagash DI. Plane-strain propagation of a fluid-driven fracture during injection and shut-in: Asymptotics of large toughness. *Engineering Fracture Mechanics* 2006; **73**:456—481.
15. Perkins TK, Kern LR. Widths of hydraulic fractures. *Society of Petroleum Engineers Journal* 1961; **89**:937–949.

16. Nordgren RP. Propagation of a vertical hydraulic fracture. *Society of Petroleum Engineers Journal* 1972; **12**:306–314.
17. Simonson ER, Abou-Sayed AS, Clifton RJ. Containment of massive hydraulic fractures. *Society of Petroleum Engineers Journal* 1978; **18**:27–32.
18. Clifton RJ, Abou-Sayed AS. A variational approach to the prediction of the three-dimensional geometry of hydraulic fractures. *SPE/DOE Low Permeability Symposium*, 1981; 457–463.
19. Clifton RJ, Wang JJ. Adaptive optimal mesh generator for hydraulic fracturing modeling. *Rock Mechanics as a Multidisciplinary Science*, Roegiers JC (ed.). Taylor & Francis Group, Balkema, Rotterdam, 1991; 607–616.
20. Barree RD. A practical numerical simulator for three-dimensional fracture propagation in heterogeneous media. *Reservoir Simulation Symposium*, 1983; 403–411.
21. Carter BJ, Desroches J, Ingraffea AR, Wawrzynek PA. Simulating fully 3D hydraulic fracturing. *Modeling in Geomechanics*, Zaman M, Gioda G, Booker J (eds.). Wiley, 2000.
22. Siebrits E, Peirce AP. An efficient multi-layer planar 3D fracture growth algorithm using a fixed mesh approach. *International Journal for Numerical Methods in Engineering* 2002; **53**:691–717.
23. Crouch SL, Starfield AM. *Boundary element methods in solid mechanics*. Unwin & Hyman: London, 1990.
24. Biot MA. General theory of three-dimensional consolidation. *Journal of Applied Physics* 1941; **12**:155–164.
25. Boone TJ, Ingraffea AR, Roegiers JC. Simulation of hydraulic fracture propagation in poroelastic rock with application to stress measurement techniques. *International Journal of Rock Mechanics and Mining Sciences and Geomechanics Abstracts* 1991; **28**:1–14.
26. Gordeyev YN. Growth of a crack produced by hydraulic fracture in a poroelastic medium. *International Journal of Rock Mechanics and Mining Sciences and Geomechanics Abstracts* 1993; **30**:233–238.
27. Lecampion B. An extended finite element method for hydraulic fracture problems. *Communications in Numerical Methods in Engineering* 2009; **25**:121–133.
28. Dahi-Taleghani A. Analysis of hydraulic fracture propagation in fractured reservoirs: an improved model for the interaction between induced and natural fractures. PhD Thesis, University of Texas, Austin 2009.
29. Adachi J, Detournay E. Plane strain propagation of a hydraulic fracture in a permeable rock. *Engineering Fracture Mechanics* 2008; **75**:4666–4694.
30. White F. *Fluid Mechanics*. WCB McGraw-Hill, 1984.
31. Moës N, Gravouil A, Belytschko T. Non-planar 3D crack growth by the extended finite element and level sets–Part I: Mechanical model. *International Journal for Numerical Methods in Engineering* 2002; **53**:2549–2568.
32. Gosz M, Moran B. An interaction energy integral method for computation of mixed-mode stress intensity factors along non-planar crack fronts in three dimensions. *Engineering Fracture Mechanics* 2002; **69**:299—319.
33. Béchet E, Minnebo H, Moës N, Burgardt B. Improved implementation and robustness study of the X-FEM for stress analysis around cracks. *International Journal for Numerical Methods in Engineering* 2005; **64**:1033–1056.
34. Fries TP. A corrected XFEM approximation without problems in blending elements. *International Journal for Numerical Methods in Engineering* 2008; **75**:503–532.
35. Shen Y, Lew A. An optimally convergent discontinuous-Galerkin-based extended finite element method for fracture mechanics. *International Journal for Numerical Methods in Engineering* 2010; **82**:716–755.
36. Givoli D, Keller JB. A finite element method for large domains. *Computer Methods in Applied Mechanics and Engineering* 1989; **76**:41–66.
37. Bettess P. Infinite elements. *International Journal for Numerical Methods in Engineering* 1977; **11**:53–64.
38. Carey GF. Derivative calculation from finite element solutions. *Computer Methods in Applied Mechanics and Engineering* 1982; **35**:1–14.
39. Dowell M, Jarratt P. A modified Regula Falsi method for computing the root of an equation. *BIT Numerical Mathematics* 1971; **11**:168–174.
40. Dowell M, Jarratt P. The "Pegasus" method for computing the root of an equation. *BIT Numerical Mathematics* 1972; **12**:503–508.